Limits on low energy photon-photon scattering from an experiment on magnetic vacuum birefringence

M. Bregant,[1] G. Cantatore,[1] S. Carusotto,[2] R. Cimino,[3] F. Della Valle,[1] G. Di Domenico,[4] U. Gastaldi,[5] M. Karuza,[6] V. Lozza,[1] E. Milotti,[1] E. Polacco,[2] G. Raiteri,[1] G. Ruoso,[5] E. Zavattini,[1,*] and G. Zavattini[4,+]

(PVLAS Collaboration)

[1]*INFN, Sezione di Trieste and Dipartimento di Fisica, Università di Trieste, Via Valerio 2, 34127 Trieste, Italy*
[2]*INFN, Sezione di Pisa and Dipartimento di Fisica, Università di Pisa, Via Buonarroti 2, 56100 Pisa Italy*
[3]*INFN, Laboratori Nazionali di Frascati, Via E. Fermi 40, 00044 Frascati, Italy*
[4]*INFN, Sezione di Ferrara and Dipartimento di Fisica, Università di Ferrara, Polo Scientifico, Via Saragat 1 C, 44100 Ferrara, Italy*
[5]*INFN, Laboratori Nazionali di Legnaro, viale dell'Università 2, 35020 Legnaro, Italy*
[6]*INFN, Sezione di Trieste, Via Valerio 2, 34127 Trieste, Italy*

(Received 20 May 2008; published 12 August 2008)

Experimental bounds on induced vacuum magnetic birefringence can be used to improve present photon-photon scattering limits in the electronvolt energy range. Measurements with the Polarizzazione del Vuoto con Laser apparatus [E. Zavattini *et al.*, Phys. Rev. D **77**, 032006 (2008)] at both $\lambda = 1064$ and 532 nm lead to bounds on the parameter A_e, describing nonlinear effects in QED, of $A_e^{(1064)} < 6.6 \times 10^{-21}$ T^{-2}@1064 nm and $A_e^{(532)} < 6.3 \times 10^{-21}$ T^{-2}@532 nm, respectively, at 95% confidence level, compared to the predicted value of $A_e = 1.32 \times 10^{-24}$ T^{-2}. The total photon-photon scattering cross section may also be expressed in terms of A_e, setting bounds for unpolarized light of $\sigma_{\gamma\gamma}^{(1064)} < 4.6 \times 10^{-62}$ m^2 and $\sigma_{\gamma\gamma}^{(532)} < 2.7 \times 10^{-60}$ m^2. Compared to the expected QED scattering cross section these results are a factor of $\simeq 2 \times 10^7$ higher and represent an improvement of a factor about 500 on previous bounds based on ellipticity measurements and of a factor of about 10^{10} on bounds based on direct stimulated scattering measurements.

DOI: 10.1103/PhysRevD.78.032006 PACS numbers: 12.20.Fv, 07.60.Fs, 42.50.Xa

I. INTRODUCTION

Classical electrodynamics in vacuum is a linear theory and does not foresee photon-photon scattering or other nonlinear effects between electromagnetic fields. Before quantum electrodynamics (QED) was formally complete, Euler and Heisenberg, and Weisskopf, realized that vacuum fluctuations, permitted by the uncertainty principle, lead to nonlinear effects: 4 photons can couple via fermion loops. Such nonlinear effects were first calculated in 1936 [1] and can be described by an effective Lagrangian L_{EHW} which, for field strengths well below their critical values ($B \ll B_{\mathrm{crit}} = m^2c^2/e\hbar = 4.4 \times 10^9$ T, $E \ll E_{\mathrm{crit}} = m^2c^3/e\hbar = 1.3 \times 10^{18}$ V/m) and for photon energies below the electron mass, can be written as (in S.I. units):

$$L_{\mathrm{EHW}} = \frac{A_e}{\mu_0}\left[\left(\frac{E^2}{c^2} - B^2\right)^2 + 7\left(\frac{\vec{E}}{c}\cdot\vec{B}\right)^2\right], \qquad (1)$$

where the parameter A_e describing the nonlinearity is

$$A_e = \frac{2}{45\mu_0}\frac{\alpha^2\lambda\!\!\!^{-3}_e}{m_e c^2} = 1.32 \times 10^{-24}\ \mathrm{T}^{-2}, \qquad (2)$$

with $\lambda\!\!\!^{-}_e$ being the Compton wavelength of the electron, $\alpha = e^2/(\hbar c 4\pi\epsilon_0)$ the fine structure constant, m_e the electron mass, c the speed of light in vacuum and μ_0 the magnetic permeability of vacuum.

Maxwell's equations are still valid provided the constitutive equations are applied to the total Lagrangian density $L = L_{\mathrm{Class}} + L_{\mathrm{EHW}}$ to derive the displacement vector $\vec{D}$ and the magnetic field intensity vector $\vec{H}$:

$$\vec{D} = \frac{1}{\epsilon_0}\frac{\partial L}{\partial \vec{E}}, \qquad \vec{H} = -\mu_0\frac{\partial L}{\partial \vec{B}}. \qquad (3)$$

One of the yet to be measured effects predicted by the L_{EHW} correction is that vacuum will become birefringent in the presence of an external magnetic and/or electric field. For example, in the case of a beam propagating perpendicularly to an external magnetic field, if $n_\parallel$ and $n_\perp$ indicate the index of refraction for polarizations, respectively, parallel and perpendicular to the field direction, the birefringence can be expressed as [2,3]

$$n_\parallel - n_\perp = \Delta n^{(\mathrm{QED})} = 3A_e B^2, \qquad (4)$$

which is extremely small: with a field intensity of 5 T,

*Deceased.
+Corresponding author.
zavattini@fe.infn.it

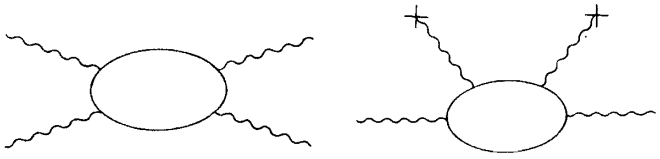

FIG. 1. First-order Feynman diagrams for both photon-photon scattering and magnetically (electrically) induced vacuum birefringence.

$\Delta n^{(\mathrm{QED})} \approx 10^{-22}$. Another process described by the same Feynman diagrams as magnetically induced vacuum birefringence is photon-photon scattering. Figure 1 shows the Feynman diagrams for both photon-photon scattering and field-induced vacuum birefringence. In general, the connection between the index of refraction n of a medium and the photon scattering amplitude in the forward direction for photons with energy E_γ, $f(\vartheta = 0, E_\gamma)$, is (see, for example, [4])

$$n = 1 + \frac{2\pi}{k^2} N f(0, E_\gamma), \tag{5}$$

where N is the average number density of centers of scattering and k is the photon wave number. Applied to photon-photon scattering of linearly polarized photons, the center of mass forward scattering amplitude of ingoing and outgoing photons all having parallel polarizations, $f_\parallel^{(\mathrm{QED})}(0, E_\gamma)$, and the one in which the two incoming photons have perpendicular polarizations as do the outgoing photons, $f_\perp^{(\mathrm{QED})}(0, E_\gamma)$, are, respectively [5],

$$f_\parallel^{(\mathrm{QED})}(0, E_\gamma) = \frac{32}{45} \frac{\alpha^2 \lambda\!\!\!^{-}_e}{4\pi} \left(\frac{E_\gamma}{m_e c^2}\right)^3 = \frac{16\mu_0}{4\pi\hbar^2 c^2} A_e {E_\gamma}^3, \tag{6}$$

$$f_\perp^{(\mathrm{QED})}(0, E_\gamma) = \frac{56}{45} \frac{\alpha^2 \lambda\!\!\!^{-}_e}{4\pi} \left(\frac{E_\gamma}{m_e c^2}\right)^3 = \frac{28\mu_0}{4\pi\hbar^2 c^2} A_e {E_\gamma}^3, \tag{7}$$

where it is apparent that the scattering amplitude is proportional to A_e. The authors of Ref. [5] also show that N is proportional to the energy density of the scatterer field (electric and/or magnetic) and inversely proportional to the photon energy in the center of mass reference frame. From the scattering amplitude one can find the differential cross section

$$\frac{d\sigma_{\gamma\gamma}}{d\Omega}(\vartheta, E_\gamma) = |f(\vartheta, E_\gamma)|^2 \tag{8}$$

and the total cross section which depends on A_e^2. For unpolarized light one finds [6–10]

$$\sigma_{\gamma\gamma}^{(\mathrm{QED})}(E_\gamma) = \frac{1}{45^2} \frac{973}{5\pi} \alpha^4 \left(\frac{E_\gamma}{m_e c^2}\right)^6 \lambda\!\!\!^{-2}_e = \frac{973\mu_0^2}{20\pi} \frac{E_\gamma^6}{\hbar^4 c^4} A_e^2. \tag{9}$$

The connection between the total photon-photon cross section and vacuum birefringence, hence the parameter A_e describing nonlinear QED effects, makes nonlinear QED searches via ellipsometric techniques very attractive. Limits on A_e from ellipsometric data can therefore be directly translated into photon-photon scattering limits.

It is interesting to note that in a post-Maxwellian framework [11] the Lagrangian density L_{pM} describing nonlinear electrodynamic effects in vacuum is parametrized by three parameters ξ, η_1 and η_2:

$$L_{\mathrm{pM}} = \frac{\xi}{2\mu_0} \left[\eta_1 \left(\frac{E^2}{c^2} - B^2\right)^2 + 4\eta_2 \left(\frac{\vec{E}}{c} \cdot \vec{B}\right)^2 \right]. \tag{10}$$

In this parametrization $\xi = 1/B_{\mathrm{crit}}^2$, and η_1 and η_2 are dimensionless parameters depending on the chosen model. In the Euler-Heisenberg electrodynamics $\eta_2^{(\mathrm{QED})} = \frac{7}{4}\eta_1^{(\mathrm{QED})} = \alpha/(45\pi)$, α being the fine structure constant.

By substituting the post-Maxwellian generalization into Eqs. (3) one finds that the birefringence induced by a transverse magnetic field is [to be compared with Eq. (4)]

$$\Delta n^{(\mathrm{pM})} = 2\xi(\eta_2 - \eta_1) B^2, \tag{11}$$

whereas the forward scattering amplitudes given in expressions (6) and (7) become

$$f_\parallel^{(\mathrm{pM})}(0, E_\gamma) = \frac{8\mu_0}{4\pi\hbar^2 c^2} \xi \eta_1 {E_\gamma}^3, \tag{12}$$

$$f_\perp^{(\mathrm{pM})}(0, E_\gamma) = \frac{8\mu_0}{4\pi\hbar^2 c^2} \xi \eta_2 {E_\gamma}^3. \tag{13}$$

Birefringence is therefore only sensitive to the difference $\eta_2 - \eta_1$ whereas the two forward scattering amplitudes $f_\parallel^{(\mathrm{pM})}(0, E_\gamma)$ and $f_\perp^{(\mathrm{pM})}(0, E_\gamma)$ are proportional, respectively, to η_1 and η_2. At scattering angles different from $\vartheta = 0$ it remains true that $f_\parallel^{(\mathrm{pM})}(\vartheta, E_\gamma)$ is proportional to η_1 but $f_\perp^{(\mathrm{pM})}(\vartheta, E_\gamma)$ will now depend on a combination of η_1 and η_2 which never cancels. Therefore, for example, in the Born-Infeld model [12] where $\eta_1 = \eta_2$, magnetically induced birefringence is not expected even though photon-photon scattering is. Although very promising for detecting nonlinear electrodynamic effects, the ellipsometric technique alone it is not sufficient to determine the two independent quantities $\xi\eta_1$ and $\xi\eta_2$. On the other hand, direct photon-photon scattering with defined polarization states can. It is clear how both techniques are complementary.

Assuming the Euler-Heisenberg Lagrangian density, in this paper we will present the best limits on $\sigma_{\gamma\gamma}$ at low energy available today.

II. APPARATUS AND METHOD

The general scheme of a sensitive ellipsometer searching for magnetically induced birefringence is presented in Fig. 2. A polarizer defines the polarization of the beam, of power I_{in}, before it enters the magnetic field region where it acquires an ellipticity ψ. The ellipticity is made time-

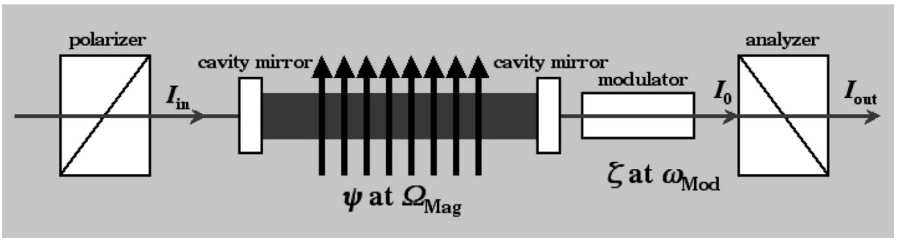

FIG. 2. Schematic layout of a sensitive ellipsometer. See text for description.

dependent by modulating the magnetic field with angular frequency Ω_{Mag} (see text below). Two mirrors compose either a multipass or a Fabry-Perot cavity to increase the optical path within the magnetic field region. The beam then passes first through a modulator, where it acquires a known ellipticity ζ modulated at frequency ω_{Mod}, and then through an analyzer. The transmitted power I_{out} is then detected and analyzed.

A. Heterodyne technique

For the purpose of our discussion let a laser beam propagate along the Z axis and let the incoming (linear) polarization define the X axis (Fig. 3). Considering the coherence of our light source, the Jones matrix formalism will be used [13]. The Jones matrix for a uniaxial birefringent element is given by

$$\mathbf{B}\,\mathbf{F}(\vartheta) = \begin{pmatrix} 1 + \imath\psi\cos2\vartheta & \imath\psi\sin2\vartheta \\ \imath\psi\sin2\vartheta & 1 - \imath\psi\cos2\vartheta \end{pmatrix}, \tag{14}$$

where ϑ represents the angle between the slow axis ($n_{\parallel} > n_{\perp}$) of the medium and the X axis and $\psi \ll 1$ is the induced ellipticity acquired by the light, given by

$$\psi = \frac{\varphi_{\parallel} - \varphi_{\perp}}{2} = \pi\frac{L(n_{\parallel} - n_{\perp})}{\lambda}, \tag{15}$$

with $\varphi_{\parallel} - \varphi_{\perp}$ the phase delay between the parallel and perpendicular polarization components acquired in a length L.

Given an input beam whose electric field after the entrance polarizer is

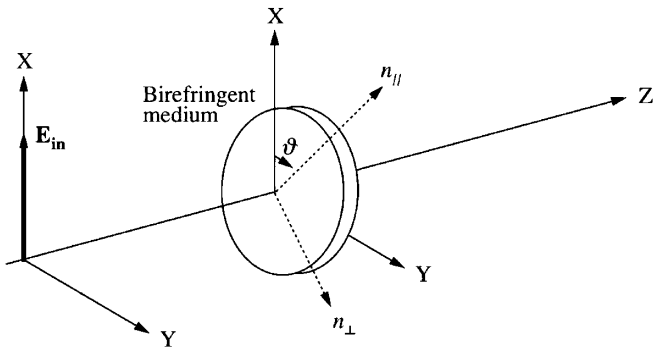

FIG. 3. Reference frame for the calculations using the Jones matrix formalism.

$$\vec{E}_{\mathrm{in}} = E_{\mathrm{in}}\begin{pmatrix} 1 \\ 0 \end{pmatrix},$$

the electric field after the birefringent medium will be

$$\vec{E}_0 = E_{\mathrm{in}} \cdot \mathbf{BF} \cdot \begin{pmatrix} 1 \\ 0 \end{pmatrix} = E_{\mathrm{in}}\begin{pmatrix} 1 + \imath\psi\cos2\vartheta \\ \imath\psi\sin2\vartheta \end{pmatrix}.$$

Assuming no losses, the power I_{out} after the analyzer (polarizer crossed with respect to the entrance polarizer) will therefore be

$$I_{\mathrm{out}} = I_{\mathrm{in}}|\imath\psi\sin2\vartheta|^2. \tag{16}$$

The power is proportional to ψ^2 and, whether ϑ is constant in time or not, results in an unmeasurably small intensity component.

To linearize the term proportional to the ellipticity signal ψ to be detected, one can add a known time-varying ellipticity $\zeta(t)$ using an ellipticity modulator. The Jones matrix for the modulator is the same as **BF** set at an angle of $\pi/4$ ($\psi \ll \zeta \ll 1$):

$$\mathbf{M}\,\mathbf{OD} = \begin{pmatrix} 1 & \imath\zeta(t) \\ \imath\zeta(t) & 1 \end{pmatrix}, \tag{17}$$

and the resulting vector describing the electric field after the modulator will be

$$\vec{E}_0 = E_{\mathrm{in}} \cdot \mathbf{MOD} \cdot \mathbf{BF} \cdot \begin{pmatrix} 1 \\ 0 \end{pmatrix} \tag{18}$$

$$= E_{\mathrm{in}}\begin{pmatrix} 1 + \imath\psi\cos2\vartheta - \psi\zeta(t)\sin2\vartheta \\ \imath\zeta(t) + \imath\psi\sin2\vartheta - \zeta(t)\psi\cos2\vartheta \end{pmatrix}. \tag{19}$$

Neglecting second-order terms, the power I_{out} after the analyzer will be

$$\begin{aligned} I_{\mathrm{out}}(t) &= I_{\mathrm{in}}|\imath\zeta(t) + \imath\psi\sin2\vartheta|^2 \\ &\simeq I_{\mathrm{in}}[\zeta(t)^2 + 2\zeta(t)\psi\sin2\vartheta], \end{aligned} \tag{20}$$

which now depends linearly on the ellipticity ψ. To complete the discussion, one finds experimentally that static and slowly varying ellipticities, in the following indicated as $\alpha(t)$, are always present in an actual apparatus and that two crossed polarizers have an intrinsic extinction ratio σ^2, mainly due to imperfections in the crystals of which they are made. Furthermore, losses in the system reduce the total light reaching the analyzer. Therefore, taking into

account an additional spurious ellipticity term $\alpha(t)$ (since $\alpha, \psi, \zeta \ll 1$ these terms commute and therefore add up algebraically) and a term proportional to σ^2, the total power at the output of the analyzer will be

$$I_{\text{out}}(t) = I_0[\sigma^2 + |\imath\zeta(t) + \imath\psi \sin 2\vartheta + \imath\alpha(t)|^2] \simeq I_0[\sigma^2 + \zeta(t)^2 + \alpha(t)^2 + 2\zeta(t)\psi \sin 2\vartheta + 2\zeta(t)\alpha(t)], \quad (21)$$

where I_0 represents the power of light reaching the analyzer.

To be able to distinguish the term $\zeta(t)\alpha(t)$, which is usually largest at low frequencies, from the term $\zeta(t)\psi \sin 2\vartheta$, the term of interest $\psi \sin 2\vartheta$ is also made to vary in time. This can be done either by ramping the magnetic field intensity (varying therefore ψ) or by rotating the magnetic field direction (varying ϑ). The final expression, explicitly indicating the time dependence of ψ and ϑ, for the power at the output of the analyzer is therefore

$$I_{\text{out}}(t) = I_0[\sigma^2 + \zeta(t)^2 + \alpha(t)^2 + 2\zeta(t)\psi(t) \sin 2\vartheta(t) + 2\zeta(t)\alpha(t)]. \quad (22)$$

B. Optical path multiplier

To further increase the ellipticity induced by the birefringent region one can increase the number of passes through it. Either a multipass cavity or a Fabry-Perot cavity can be used for this purpose. In the Polarizzazione del Vuoto con Laser (PVLAS) experiment described below, Fabry-Perot has been chosen. In a multipass cavity the induced ellipticity is proportional to the number of passes N_{pass} through the region. With a Fabry-Perot cavity the calculation is not immediate since one is dealing with a standing wave.

Let t and r be the transmission and reflection coefficients, respectively, and p the losses of the mirrors of the cavity such that $t^2 + r^2 + p = 1$. Let d be the length of the cavity and $\delta = 4\pi d/\lambda$ the round-trip phase for a beam of wavelength λ. Then the Jones matrix for the elements of the ellipsometer after the entrance polarizer is

$$\mathbf{E\,LL} = \mathbf{A} \cdot \mathbf{SP} \cdot \mathbf{MOD} \cdot t^2 e^{\imath\delta/2} \sum_{n=0}^{\infty} [\mathbf{BF}^2 r^2 e^{\imath\delta}]^n \cdot \mathbf{BF}, \quad (23)$$

where

$$\mathbf{A} = \begin{pmatrix} 0 & 0 \\ 0 & 1 \end{pmatrix}$$

is the analyzer Jones matrix and **SP** describes the spurious ellipticity. Because $r^2 < 1$, **ELL** can be rewritten as

TABLE I. Intensity of the frequency components of the signal after the analyzer **A**.

Frequency	Fourier component	Intensity/I_0	Phase
dc	I_{dc}	$\sigma^2 + \alpha_{\text{dc}}^2 + \zeta_0^2/2$	$\cdots$
ω_{Mod}	$I_{\omega_{\text{Mod}}}$	$2\alpha_{\text{dc}}\zeta_0$	θ_{Mod}
$\omega_{\text{Mod}} \pm 2\Omega_{\text{Mag}}$	$I_{\omega_{\text{Mod}} \pm 2\Omega_{\text{Mag}}}$	$\zeta_0 \frac{2\mathcal{F}}{\pi}\psi$	$\theta_{\text{Mod}} \pm 2\theta_{\text{Mag}}$
$2\omega_{\text{Mod}}$	$I_{2\omega_{\text{Mod}}}$	$\zeta_0^2/2$	$2\theta_{\text{Mod}}$

$$\mathbf{E\,LL} = \mathbf{A} \cdot \mathbf{SP} \cdot \mathbf{MOD} \cdot t^2 e^{\imath\delta/2} [\mathbf{I} - \mathbf{BF}^2 r^2 e^{\imath\delta}]^{-1} \cdot \mathbf{BF}, \quad (24)$$

with **I** the identity matrix. With the laser phase locked to the cavity so that $\delta = 2\pi m$, where m is an integer number, the electric field at the output of the system will be

$$\vec{E}_{\text{out}} = E_{\text{in}} \cdot \mathbf{ELL} \cdot \begin{pmatrix} 1 \\ 0 \end{pmatrix} = E_{\text{in}} \frac{t^2}{t^2 + p} \begin{pmatrix} 0 \\ \imath\alpha(t) + \imath\zeta(t) + \imath\frac{1+r^2}{1-r^2}\psi \sin 2\vartheta \end{pmatrix}, \quad (25)$$

and the power, including losses,

$$I_{\text{out}}(t) = I_0 \left| \imath\alpha(t) + \imath\zeta(t) + \imath\left(\frac{1+r^2}{1-r^2}\right)\psi \sin 2\vartheta \right|^2. \quad (26)$$

This expression is at the basis of the ellipsometer in the PVLAS apparatus. Small ellipticities add up algebraically and the Fabry-Perot multiplies the single pass ellipticity $\psi \sin 2\vartheta$, generated within the cavity, by a factor $(1 + r^2)/(1 - r^2) \approx 2\mathcal{F}/\pi$, where $\mathcal{F}$ is the finesse of the cavity. The ellipticity signal to be detected is therefore $\Psi = (2\mathcal{F}/\pi)\psi \sin 2\vartheta$. Typical values for the finesse $\mathcal{F}$ of the PVLAS cavity are $\simeq 10^5$.

In the PVLAS experiment, $\zeta(t) = \zeta_0 \cos(\omega_{\text{Mod}} t + \theta_{\text{Mod}})$ and the magnetic field direction is rotated at an angular velocity Ω_{Mag}. A Fourier analysis of the power $I_{\text{out}}(t)$ of Eq. (26) results in four main frequency components each with a definite amplitude and phase. These are reported in Table I.

The presence of a component at $\omega_{\text{Mod}} \pm 2\Omega_{\text{Mag}}$ in the signal identifies an induced ellipticity within the Fabry-Perot cavity. Furthermore the phase of this component must satisfy the value in Table I.

C. PVLAS apparatus

A description of the PVLAS apparatus, shown schematically in Fig. 4, can be found in Refs. [14–16]. The magnetic field is provided by a superconducting dipole magnet which is placed vertically and rotates around its axis, at a typical frequency of 0.3 Hz. The magnetic field therefore lies in the horizontal plane, the field region is 1 m long, and the maximum field intensity is 5.5 T. The ellipsometer

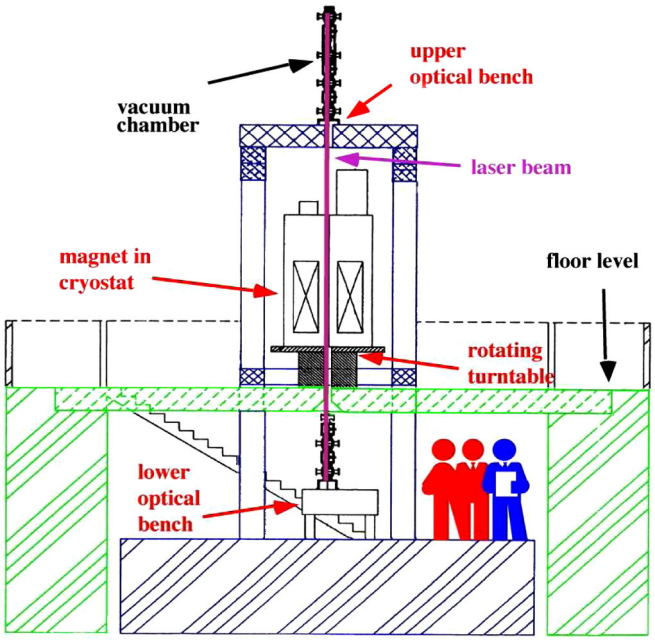

FIG. 4 (color online). Schematic layout of the PVLAS apparatus. See text for description.

develops vertically: the polarizer and entrance cavity mirror are supported by the lower optical bench, whereas the output cavity mirror, modulator and analyzer are in a vacuum chamber on the upper optical bench. The lower optical bench is in a pit whose floor is a concrete slab resting on four 14 m long pillars buried in the ground. The slab and pillars are therefore seismically isolated with respect to the surrounding hall floor and building. The upper optical bench is sustained by a granite tower 7 m high also standing on the concrete slab. The upper and lower vacuum chambers are connected by a quartz tube 2.5 cm in diameter which passes through the warm bore of the cryostat containing the magnet. The magnet and turntable are supported by a concrete beam crossing over the pit and resting on the hall floor. Thus, mechanical vibrations due to the rotating magnet reaching the optical system will be greatly suppressed and should not cause excess ellipticity noise.

The vacuum system is based on two liquid N_2 traps combined with a Ti sublimation getter, and pressure is kept at the level of $P \approx 10^{-8}$ mbar during measurements. For test purposes the vacuum chamber can be filled with gases at known pressure, measured with a set of capacitive transducers. The presence of the gas gives rise to a known magnetic birefringence via the Cotton-Mouton effect [17–19].

The laser source is frequency locked to the Fabry-Perot cavity using a modified Pound-Drever-Hall technique [20]. Two different light sources were alternatively used: an infrared Nd:YAG laser emitting 800 mW at 1064 nm (infrared) and its frequency doubled secondary output of 80 mW at 532 nm (green). The cavity parameters were as follows: finesse $\mathcal{F}_{1064} = 70\,000$ and output power $P_{1064} = 60$ mW for the infrared and $\mathcal{F}_{532} = 37\,000$ and $P_{532} = 1.5$ mW for the green.

The light transmitted by the analyzer is detected by a photodiode connected to a low noise current amplifier and the signal is then sent to both a spectrum analyzer, for online monitoring of the apparatus, and to a lock-in amplifier demodulated at ω_{Mod}. To make the analysis independent from the instability of the rotation frequency of the turntable sustaining the magnet, the table perimeter is equipped with 32 equally spaced trigger marks. The output of the lock-in amplifier is acquired at the passage of each trigger mark, therefore maintaining the coherence of the searched signal even for long integration times.

D. Noise considerations

In the presence of a signal above background with the correct Fourier phase, the ellipticity $\Psi = (2\mathcal{F}/\pi)\psi$ can be calculated from I_0, from the Fourier components $I_{\omega_{\mathrm{Mod}} \pm 2\Omega_{\mathrm{Mag}}}$, and from $I_{2\omega_{\mathrm{Mod}}}$ as the average of the two sideband signals:

$$\Psi = \frac{1}{2}\left(\frac{I_{\omega_{\mathrm{Mod}}+2\Omega_{\mathrm{Mag}}}}{\sqrt{2I_0 I_{2\omega_{\mathrm{Mod}}}}} + \frac{I_{\omega_{\mathrm{Mod}}-2\Omega_{\mathrm{Mag}}}}{\sqrt{2I_0 I_{2\omega_{\mathrm{Mod}}}}}\right). \tag{27}$$

Indicating with $R_{\omega_{\mathrm{Mod}} \pm 2\Omega_{\mathrm{Mag}}}$ the noise spectral density at the signal frequencies, and assuming $R_{\omega_{\mathrm{Mod}}+2\Omega_{\mathrm{Mag}}} = R_{\omega_{\mathrm{Mod}}-2\Omega_{\mathrm{Mag}}}$, the sensitivity spectral density Ψ_{Sens} of the ellipsometer for a unity signal to noise ratio is

$$\Psi_{\mathrm{Sens}} = \frac{R_{\omega_{\mathrm{Mod}}+2\Omega_{\mathrm{Mag}}}}{\sqrt{4I_0 I_{2\omega_{\mathrm{Mod}}}}}. \tag{28}$$

In principle the rms noise limit for such a system is determined by the rms shot noise i_{shot} of the dc current i_{dc} generated by the modulation amplitude $I_0 q \zeta_0^2/2$, by the extinction ratio $I_0 q \sigma^2$ and by the dc component of the spurious ellipticity $I_0 q \alpha_{\mathrm{dc}}^2$ (see Table I):

$$i_{\mathrm{shot}} = \sqrt{2e i_{\mathrm{dc}} \Delta\nu} = \sqrt{2eI_0 q\left(\sigma^2 + \frac{\zeta_0^2}{2} + \alpha_{\mathrm{dc}}^2\right)\Delta\nu}, \tag{29}$$

where q is the quantum efficiency of the photodetector, $\Delta\nu$ is the bandwidth and e is the electron charge. In the case $\zeta_0^2 \gg \sigma^2$ and $\zeta_0^2 \gg \alpha_{\mathrm{dc}}^2$ the dc current will depend only on ζ_0 and by substituting $R_{\omega_{\mathrm{Mod}} \pm \Omega_{\mathrm{Mag}}} = i_{\mathrm{shot}}/(q\sqrt{\Delta\nu})$ into Eq. (28) the shot-noise sensitivity spectral density Ψ_{shot} becomes

$$\Psi_{\mathrm{shot}} = \sqrt{\frac{e}{2I_0 q}}. \tag{30}$$

For a power $I_0 = 10$ mW and a quantum efficiency $q = 0.7$ A/W this leads to a sensitivity spectral density of $\Psi_{\mathrm{shot}} \simeq 3.4 \times 10^{-9}\ \frac{1}{\sqrt{\mathrm{Hz}}}$. It is interesting to note that such

TABLE II. Experimental parameters for the two laser configurations.

Configuration	Photodiode efficiency q [A/W]	Cavity output power I_0 [mW]	Extinction ratio σ^2	RIN(ω_{Mod}) [$1/\sqrt{\mathrm{Hz}}$]	Gain G [V/A]	Photodiode noise V_{dark} [$\mu\mathrm{V}/\sqrt{\mathrm{Hz}}$]
Green	0.2	1.5	5×10^{-7}	2×10^{-5}	10^9	2
Infrared	0.7	60	5×10^{-7}	2×10^{-5}	10^7	8

a limit depends exclusively on the laser power before the analyzer and the quantum efficiency of the detector.

Other intrinsic noise sources are photodiode dark current noise $i_{\mathrm{dark}} = V_{\mathrm{dark}}\sqrt{\Delta\nu}/G$, Johnson current noise $i_{\mathrm{J}} = \sqrt{4K_BT\Delta\nu/G}$ of the transimpedence G in the amplifier of the photodiode, and relative laser intensity current noise $i_{\mathrm{RIN}} = I_0 q \cdot \mathrm{RIN}(\omega)\sqrt{\Delta\nu}$. These noises must be kept below i_{shot} at a frequency near ω_{Mod} in order to reach the theoretical sensitivity. The expressions for these noise contributions to the ellipticity spectral noise density can be obtained from Eq. (28):

$$\Psi_{\mathrm{shot}} = \sqrt{\frac{e}{I_0 q}\left(\frac{\sigma^2 + \zeta_0^2/2}{\zeta_0^2}\right)}, \tag{31}$$

$$\Psi_{\mathrm{dark}} = \frac{V_{\mathrm{dark}}}{G\sqrt{2}}\frac{1}{I_0 q \zeta_0}, \tag{32}$$

$$\Psi_{\mathrm{J}} = \sqrt{\frac{2K_BT}{G}}\frac{1}{I_0 q \zeta_0}, \tag{33}$$

$$\Psi_{\mathrm{RIN}} = \frac{\mathrm{RIN}(\omega_{\mathrm{Mod}})}{\sqrt{2}}\frac{\sqrt{(\sigma^2 + \zeta_0^2/2)^2 + (\zeta_0^2/2)^2}}{\zeta_0}. \tag{34}$$

With the PVLAS experimental parameters given in Table II, the contribution of each of these noises to the sensitivity spectral density can be plotted as a function of the modulation amplitude ζ_0. This allows the optimization of the modulation amplitude. Figure 5 shows the corresponding plots for the infrared and green configurations. In each graph a cross marks the current experimental long term sensitivity.

As can be seen, in both configurations we are still well away from the theoretical limit. The one noise source which cannot, at the moment, be controlled is the low frequency spurious ellipticity $\alpha(t)$ [see Eq. (22)] induced in the system. We believe this noise is due to the movement of the granite tower. Since the mirrors and optical elements have a structural birefringence "map" with a gradient [21], these movements will generate ellipticity noise. Indeed, we have measured the induced ellipticity as a function of movement at the top of the tower and found a value $\simeq 0.4\ \mathrm{m}^{-1}$. To reach the theoretical limit, the relative movement of the top of the tower with respect to the lower optical bench must be less than $10^{-8}\ \mathrm{m}/\sqrt{\mathrm{Hz}}$.

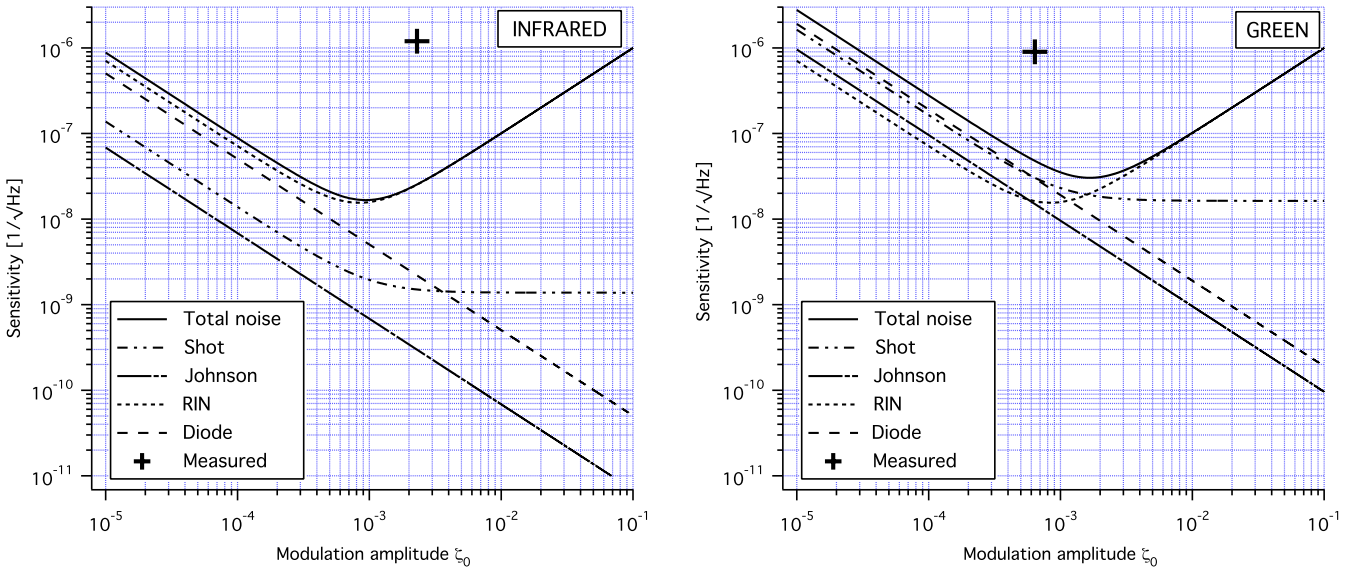

FIG. 5 (color online). Calculated and measured noise contributions for the infrared and green configurations of the PVLAS apparatus. See text and Table II for the parameters of each configuration.

III. PREVIOUS PHOTON-PHOTON SCATTERING RESULTS

In this section we review the results obtained by Bernard *et al.* in a direct search for diffused photons from two colliding beams [9] and the results from the BFRT Collaboration [22], another experiment designed to search for axions via ellipsometric techniques. There are several proposals for improving the direct scattering measurements [23–26] and for detecting the magnetic birefringence of vacuum [27–29].

A. Stimulated photon-photon scattering

In Ref. [9] direct photon-photon scattering was searched for. Differently from what was previously done [10], the authors searched for stimulated scattering when three high power ultrashort beams were crossed. The advantage of this configuration is to fix the angle and wavelength for the scattered photon: scattered photons are searched for in a defined direction and at a defined wavelength. Indeed in two-beam scattering, energy (indicated as e_i) and 3-momentum (indicated as $\mathbf{k}_i$) must be conserved: $e_1 + e_2 = e_3 + e_4$; $\mathbf{k}_1 + \mathbf{k}_2 = \mathbf{k}_3 + \mathbf{k}_4$. This leaves two free parameters for the final state. In the three-beam configuration the fourth (scattered) beam must satisfy the condition $\mathbf{k}_4 = \mathbf{k}_1 + \mathbf{k}_2 - \mathbf{k}_3$ and $\lambda_4 = (1/\lambda_1 + 1/\lambda_2 - 1/\lambda_3)^{-1}$. In the configuration being discussed $\lambda_1 = \lambda_2 = 800$ nm and $\lambda_3 = 1300$ nm, resulting in $\lambda_4 = 577$ nm.

The theoretical analysis of three-wave mixing in vacuum develops in analogy with three-wave mixing in a medium [9]. In this latter case the medium polarizability is written as

$$\mathcal{P}(t) = \underline{\chi}^{(1)}\mathcal{E}(t) + \underline{\chi}^{(2)}\mathcal{E}^2(t) + \underline{\chi}^{(3)}\mathcal{E}^3(t) + \cdots. \quad (35)$$

In four-wave mixing the authors show that the growth rate of the electric field $\mathcal{E}_{04}$ of the scattered beam depends on $\chi^{(3)}$ and can be written as

$$\frac{d\mathcal{E}_{04}}{dz} = -\frac{i\omega_4}{2c}\chi^{(3)}\mathcal{E}_{01}\mathcal{E}_{02}\mathcal{E}_{03}, \quad \text{with} \quad \frac{d}{dz} = \frac{\partial}{\partial z} + \frac{1}{c}\frac{\partial}{\partial t}. \quad (36)$$

When considering the Euler-Heisenberg Lagrangian density correction one finds that the growth rate of $\mathcal{E}_{04}$ in vacuum has the same form as Eq. (36) with the QED susceptibility of vacuum having the expression

$$\chi^{(3)} = \chi_v^{(3)} = \frac{2\hbar e^4 K}{360\pi^2 m^4 c^7 \epsilon_0} = A_e \frac{2K}{c^2} \simeq 3.0 \times 10^{-41}\ \mathrm{K\,m^2/V^2}, \quad (37)$$

where K is a parameter depending on the direction of the incident beams and their polarization. In the experiment reported in Ref. [23] $K \simeq 0.56$.

Integration of Eq. (36) leads to a number of counts per pulse crossing

$$N_4 = \epsilon_{\mathrm{PM}}\epsilon_{\mathrm{Sp}}\epsilon_{\mathrm{loss}}\frac{128}{\pi\sqrt{33}}\frac{(\hbar\omega_4)E_1E_2E_3}{e^4w^2(c\tau)^2}(\chi^{(3)})^2, \quad (38)$$

where E_i are the energies of the three incoming laser pulses, ϵ_{PM}, ϵ_{Sp}, and ϵ_{loss} are the quantum efficiency of the photomultiplier tube, the transmission of the spectrometer and a loss factor due to a beam position oscillation, respectively, and w and $c\tau$ are, respectively, the beam waist and bunch length. The value of the third-order susceptibility $\chi^{(3)}$ of nitrogen was measured and compared to other experiments. An order of magnitude agreement was observed, allowing a calibration of the apparatus. A comparison between the expected vacuum counts calculated from QED and the observed counts resulted in a limit on the total photon-photon cross section at 0.8 eV center of mass energy of

$$\sigma_{\gamma\gamma}^{(\mathrm{Bernard})} = \frac{N_{4,\mathrm{obs}}}{N_{4,\mathrm{QED}}}\sigma_{\gamma\gamma}^{(\mathrm{QED})} = 1.5 \times 10^{-52}\ \mathrm{m^2}, \quad (39)$$

which is 18 orders of magnitude larger than the theoretical QED cross section.

B. Brookhaven-Fermilab-Rochester-Trieste (BFRT) results

The principle of the ellipsometer in the BFRT Collaboration is the same as the one shown in Fig. 2. In this case the cavity was a multipass cavity with a number of reflections which varied from 34 to 578. The laser wavelength was 514.5 nm and the length of the magnetic field region was 8.8 m. To modulate the magnetic vacuum birefringence the magnetic field was ramped from 2.63 to 3.87 T at a frequency of 30 mHz. The sensitivity of the apparatus varied as a function of the number of reflections in the multipass cavity and consequently did the final limit on the acquired ellipticity. The results are summarized in Table III.

TABLE III. Summary of the BFRT experimental parameters and results together with the limit achieved on the parameter A_e.

Number of passes	Measured sensitivity $[1/\sqrt{\mathrm{Hz}}]$	Ellipticity upper bound ψ_{limit} at 95% C.L.	A_e upper bound $[T^{-2}]$
0 (shunt)	2.6×10^{-8}	7.7×10^{-10}	
34	7.9×10^{-8}	2.0×10^{-9}	1.4×10^{-19}
578	1.5×10^{-6}	5.1×10^{-8}	2.1×10^{-19}

Because of the fact that the magnetic field was ramped around a central value $B_0 = 3.25$ T, with an excursion $\pm\Delta B = \pm 0.62$ T, the expression for the Euler-Heisenberg induced magnetic birefringence is

$$\Delta n = 3A_e(2B_0\Delta B), \tag{40}$$

and the limit on A_e attainable from the BFRT results is

$$A_e < \psi_{\text{limit}} \frac{\lambda}{6B_0\Delta BNL}. \tag{41}$$

When translated into a photon-photon cross section for unpolarized light these results give a limit of

$$\sigma_{\gamma\gamma}^{(\text{BFRT})} < 1.6 \times 10^{-57}\ \text{m}^2. \tag{42}$$

This must be compared to the QED photon-photon cross section at the same wavelength of 514.5 nm which is $\sigma_{\gamma\gamma}^{(\text{QED})} = 1.44 \times 10^{-67}\ \text{m}^2$.

IV. PVLAS RESULTS

Gas measurements, for calibration, and vacuum birefringence measurements were conducted with the apparatus in both the infrared and the green configurations. We present here measurements taken with the magnet energized at 2.3 T. This choice of field strength is motivated by the strong suppression of the stray field outside the magnet. Indeed, at higher fields the presence of a stray field has resulted in a yet to be understood spurious ellipticity signal [16]. The total integration times were $T_{1064} = 45\,200$ s at 1064 nm and $T_{532} = 28\,300$ s at 532 nm.

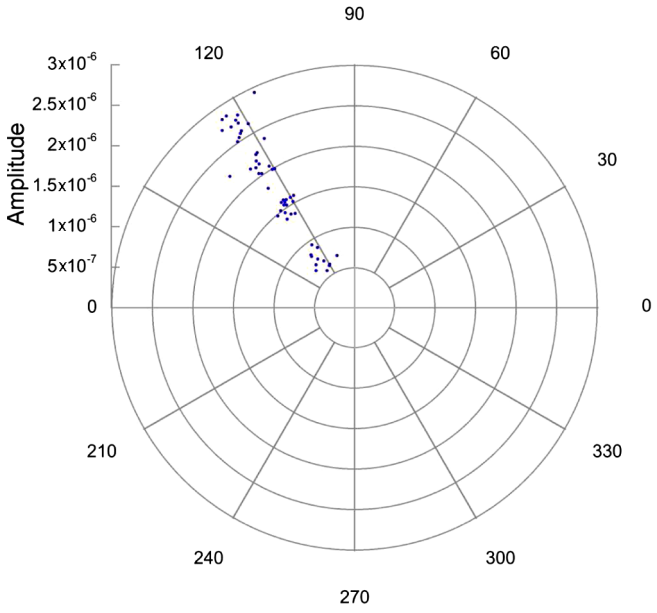

FIG. 6 (color online). Polar plot for the ellipticity signal generated with a 2.3 T magnetic field intensity when helium gas is present in the vacuum chamber. The figure shows the signal for four different gas pressures: 5, 10, 15 and 20 mbar. Each data point represents the amplitude and phase of the signal peak observed in a 100 s long time record. This figure was already published as Fig. 3 in our previous paper cited in Ref. [16].

A. Gas calibration measurements

Calibration of the ellipsometer is done by taking advantage of the Cotton-Mouton effect [17] in gases. In the presence of an external magnetic field perpendicular to the propagation of a light beam, gases become birefringent. Depending on the gas, the induced birefringence may be positive ($n_\parallel - n_\perp > 0$; e.g. He) or negative ($n_\parallel - n_\perp < 0$; e.g. N_2). These measurements also allow the verification of the Fourier phase of the sidebands of ω_{Mod} at $\omega_{\text{Mod}} \pm 2\Omega_{\text{Mag}}$ with what they should be (see Table I). Indeed, the ellipticity induced by a birefringence is maximum when the angle between the polarization and the slow axis defined by the magnetic field is 45° ($n_\parallel - n_\perp > 0$). Figure 6 shows a polar plot corresponding to the amplitude and phase of the signal demodulated at ω_{Mod} due to helium gas at four different pressures (5, 10, 15 and 20 mbar), measured with a field intensity of 2.3 T. As can be seen, the experimental values lie on a straight line with a Fourier phase of 125°. This defines the physical axis of signals. A gas with a negative Cotton-Mouton constant would generate a signal at 180° with respect to the signals shown in Fig. 6.

Different gases were measured [18,19] resulting in an accuracy better than 20%.

B. Vacuum measurements

The complete data sets of the signals from the lock-in amplifiers demodulated at ω_{Mod} were analyzed by a Fourier transform. No peak was found at $2\Omega_{\text{Mag}}$ as would be expected from a magnetically induced ellipticity. The data will therefore be presented as a noise histogram in a frequency band around $2\Omega_{\text{Mag}}$, between $1.92\Omega_{\text{Mag}}$ and $2.08\Omega_{\text{Mag}}$ (see Fig. 7).

The probability density function for the Fourier amplitude $r_{\text{F}} = \sqrt{x_{\text{F}}^2 + y_{\text{F}}^2}$, where x_{F} and y_{F} are the projections of the Fourier transform along the physical and the nonphysical phases (defined above), respectively, is given by the Rayleigh distribution $p(r_{\text{F}}) = r_{\text{F}} e^{-(r_{\text{F}}^2/2\sigma^2)}/\sigma^2$. In this expression σ is the standard deviation of the Gaussian noise distributions of x_{F} and y_{F} from which we deduced our limits on the induced ellipticity. To extract σ from the histograms the r_{F} noise distributions were fitted with the Rayleigh distribution.

The 95% confidence limits are then deduced from the cumulative distribution $P(r_{\text{F}}) = 1 - e^{-r_{\text{F}}^2/2\sigma^2}$. In Fig. 7 are shown the histograms and fits for the measurements taken with the 1064 and 532 nm lasers. Superimposed on these graphs, represented by a vertical black line, are the values at the bins corresponding to $2\Omega_{\text{Mag}}$ of the Fourier spectrum of the demodulated signal. As can be seen, these are well

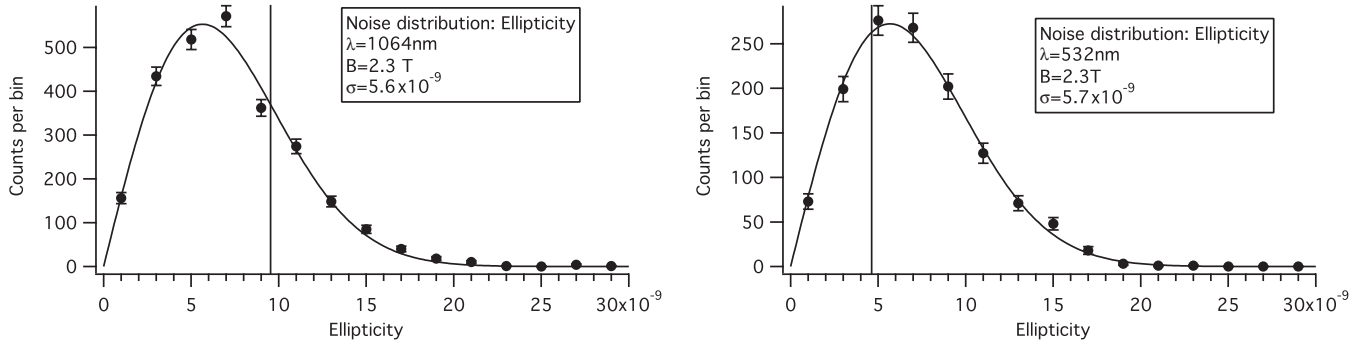

FIG. 7. Noise distributions in the magnet rotation frequency band $1.92\ \Omega_{\mathrm{Mag}} - 2.08_{\mathrm{Mag}}$ for the 2.3 T ellipticity measurements with the IR (left) laser and the green (right) laser. The vertical line indicates the value in the Fourier spectrum corresponding to $2\Omega_{\mathrm{Mag}}$. Indicated in the legend is the value of σ for the two wavelengths. The figure on the left was already published as Fig. 7 (left) in our previous paper cited in Ref. [16].

TABLE IV. Ellipticity results and stimulated scatter results for $\sigma_{\gamma\gamma}$.

Measurement type	Photon energy	Noise floor	$(B^2l)_{\mathrm{equiv}}$ [T^{2}m]	A_e bounds 95% C.L. [T^{-2}]	$\sigma_{\gamma\gamma}$ bounds [m^2]	$\sigma_{\gamma\gamma}/\sigma_{\gamma\gamma}^{(\mathrm{QED})}$
Stimulated scatter [9]	0.8 eV center of mass			1.2×10^{-15}	1.5×10^{-52}	8×10^{17}
BFRT ellipticity [22]	2.42 eV	4.9×10^{-9}	1197	1.4×10^{-19}	1.6×10^{-57}	11×10^{9}
PVLAS ellipticity [16]	1.17 eV	1.4×10^{-8}	238 000	6.6×10^{-21}	4.6×10^{-62}	2.5×10^{7}
PVLAS ellipticity	2.34 eV	1.4×10^{-8}	124 000	6.3×10^{-21}	2.7×10^{-60}	2.3×10^{7}

within the noise distributions. The standard deviations of the two distributions are very similar even though the integration time with the 532 nm laser was 70% of the integration time with the 1064 nm laser. This is due to the lower noise encountered with the 532 nm setup.

Table IV gives the 95° confidence level background values for the ellipticity measurements with the PVLAS and the BFRT apparatus. The stimulated scattering results are also reported where appropriate. The parameters for the different configurations are also reported in the same table. In the last three columns we also report the limits on A_e, $\sigma_{\gamma\gamma}$ and the ratio $\sigma_{\gamma\gamma}/\sigma_{\gamma\gamma}^{(\mathrm{QED})}$.

Although experimental results have not reached the predicted QED values, bounds have been improved. We believe that at the moment the sensitivity is limited by seismically induced spurious ellipticities.

V. DISCUSSION AND CONCLUSIONS

We have reported here the interpretation of vacuum magnetic birefringence limits in terms of photon-photon scattering. Although the sensitivity of our apparatus has not reached its theoretical shot-noise limit, the ellipsometric technique is at the moment the most sensitive one for approaching low energy nonlinear QED effects. In a general post-Maxwellian framework, though, direct scattering measurements are necessary to extract the free parameters $\xi\eta_1$ and $\xi\eta_2$ [see Eq. (10)]. In the Euler-Heisenberg framework we are now a factor of 4800 away from the theoretical parameter $A_e = 1.32 \times 10^{-24}$ T^{-2}, describing nonlinear quantum electrodynamic effects:

$$A_e^{(\mathrm{Exp})} < 6.3 \times 10^{-21}\ \mathrm{T}^{-2}@95\%\ \mathrm{C.L.} \tag{43}$$

Always in the Euler-Heisenberg framework, from the experimental bound on A_e one can place the following upper bounds on the photon-photon cross section for nonpolarized light in the limit $\hbar\omega \ll m_e c^2$, at 1064 and 532 nm, respectively, of:

$$\sigma_{\gamma\gamma}^{(1064)} < 4.6 \times 10^{-62}\ \mathrm{m}^2, \tag{44}$$

$$\sigma_{\gamma\gamma}^{(532)} < 2.7 \times 10^{-60}\ \mathrm{m}^2. \tag{45}$$

[1] H. Euler and B. Kochel, Naturwissenschaften **23**, 246 (1935); W. Heisenberg and H. Euler, Z. Phys. **98**, 714 (1936); V. S. Weisskopf, K. Dan. Vidensk. Selsk. Mat.-Fys. Medd. **14**, 6 (1936); J. Schwinger, Phys. Rev. **82**, 664 (1951).
[2] R. Baier and P. Breitenlohner, Acta Phys. Austriaca **25**, 212 (1967); R. Baier and P. Breitenlohner, Nuovo Cimento **47**, 261 (1967); S. L. Adler, Ann. Phys. (N.Y.) **67**, 599 (1971); Z. Bialynicka-Birula and I. Bialynicki-Birula, Phys. Rev. D **2**, 2341 (1970).
[3] E. Iacopini and E. Zavattini, Phys. Lett. **85B**, 151 (1979).
[4] R. G. Newton, Am. J. Phys. **44**, 639 (1976).
[5] J Haïssinski *et al.*, Phys. Scr. **74**, 678 (2006).
[6] B. De Tollis, Nuovo Cimento **35**, 1182 (1965); **32**, 757 (1964).
[7] R. Karplus *et al.*, Phys. Rev. **83**, 776 (1951).
[8] D. A. Dicus *et al.*, Phys. Rev. D **57**, 2443 (1998).
[9] D. Bernard *et al.*, Eur. Phys. J. D **10**, 141 (2000).
[10] F. Moulin *et al.*, Z. Phys. C **72**, 607 (1996).
[11] V. I. Denisov *et al.*, Phys. Rev. D **69**, 066008 (2004).
[12] M. Born, Proc. R. Soc. London **143**, 410 (1934).M. Born and L. Infeld, Proc. R. Soc. London **144**, 425 (1934).
[13] R. C. Jones, J. Opt. Soc. Am. **38**, 671 (1948); E. Hecht, *Optics* (Addison-Wesley, Reading, MA, 1987), 2nd ed.
[14] D. Bakalov *et al.*, Hyperfine Interact. **114**, 103 (1998).
[15] E. Zavattini *et al.*, Phys. Rev. Lett. **96**, 110406 (2006).
[16] E. Zavattini *et al.*, Phys. Rev. D **77**, 032006 (2008).
[17] C. Rizzo *et al.*, Int. Rev. Phys. Chem. **16**, 81 (1997).
[18] F. Brandi *et al.*, J. Opt. Soc. Am. B **15**, 1278 (1998).
[19] M. Bregant *et al.*, Chem. Phys. Lett. **392**, 276 (2004).
[20] M. Bregant *et al.*, Rev. Sci. Instrum. **73**, 4142 (2002).
[21] P. Micossi *et al.*, Appl. Phys. B **57**, 95 (1993).
[22] R. Cameron *et al.*, Phys. Rev. D **47**, 3707 (1993).
[23] E. Lundström *et al.*, Phys. Rev. Lett. **96**, 083602 (2006).
[24] D. Tommasini *et al.*, Phys. Rev. A **77**, 042101 (2008).
[25] A. N. Luiten *et al.*, Phys. Lett. A **330**, 429 (2004).
[26] A. N. Luiten *et al.*, Phys. Rev. A **70**, 033801 (2004).
[27] R. Battesti *et al.*, Eur. Phys. J. D **46**, 323 (2008).
[28] W. T. Ni, Chin. J. Phys. (Taipei) **34**, 962 (1996).
[29] P. Pugnat *et al.*, Cesk. Cas. Fyz. **56**, C193 (2006).